Molecular Switching by Proton-Coupled Electron Transport Drives Giant Negative Differential Resistance

Qian Zhang,[1,2]† Yulong Wang,[1]† Cameron Nickle,[3]† Ziyu Zhang,[1] Andrea Leoncini,[1] Dong-Chen Qi,[4] Kai Sotthewes,[5] Alessandro Borrini,[6] Harold J. W. Zandvliet,[5] Enrique del Barco,[3]* Damien Thompson,[7]* and Christian A. Nijhuis,[6]*

[1]Department of Chemistry, National University of Singapore, 3 Science Drive 3, Singapore 117543.
[2]School of Chemistry and Chemical Engineering, Chongqing University, Chongqing 400044, China.
[3]Department of Physics, University of Central Florida, Orlando, Florida 32816 - USA.
[4]Centre for Materials Science, School of Chemistry and Physics, Queensland University of Technology, Brisbane, Queensland 4001, Australia.
[5]Physics of Interfaces and Nanomaterials, MESA+ Institute for Nanotechnology, University of Twente, P.O. Box 217, 7500AE Enschede, The Netherlands
[6]Hybrid Materials for Opto-Electronics Group, Department of Molecules and Materials, MESA+ Institute for Nanotechnology, Molecules Center and Center for Brain-Inspired Nano Systems, Faculty of Science and Technology, University of Twente, 7500 AE Enschede, The Netherlands.
[7]Department of Physics, Bernal Institute, University of Limerick, Limerick V94 T9PX, Ireland.

†These authors contributed equally to this work

*Authors to whom correspondence should be addressed: c.a.nijhuis@utwente.nl, damien.thompson@ul.ie and delbarco@ucf.edu.

Abstract:

To develop new types of dynamic molecular devices with atomic-scale control over electronic function, new types of molecular switches are needed with time-dependent switching probabilities. We report such a molecular switch based on proton-coupled electron transfer (PCET) reaction with giant hysteric negative differential resistance (NDR) with peak-to-valley ratios of 120 ± 6.6 and memory on/off ratios of $(2.4 \pm 0.6) \times 10^3$. The switching dynamics probabilities are modulated by bias voltage sweep rate and can also be controlled by pH and relative humidity, confirmed by kinetic isotope effect measurements. The demonstrated dynamical and environment-specific modulation of giant NDR and memory effects provide new opportunities for bioelectronics and artificial neural networks.

2

Introduction

Concerted proton and electron transfer reactions (proton-coupled electron transfer, PCET) are ubiquitous in Nature enabling processes ranging from photosynthesis, signaling and respiration to biosynthesis and nitrogen fixation. The exquisite control and efficiency of these processes inspires the development of, for example, artificial leaves, catalysts, or fuel cells[1, 2, 3, 4], and more recently, PCET based molecular electronics[5, 6] that aims to produce electronic devices with atomic-scale control over the mechanisms of charge transport bridging chemistry and quantum physics[7, 8, 9]. Nature exploits PCET reactions ranging from distinct proton and electron transfer steps to concerted proton-electron transfer[2, 10, 11] but molecular electronic devices operate in the solid state and usually under fixed conditions lacking a proton source and so only electron transport is considered. Here, we demonstrate the expansion in materials functionality and improvement in device performance obtainable in molecular junctions by PCET. Operating at room temperature, the devices exhibit giant hysteric negative differential resistance (NDR, a decrease in current with increasing voltage) with peak-to-valley ratio $R_{PtV} = 120 \pm 6.6$ and on/off ratio $R_{on/off} = (2.4 \pm 0.6) \times 10^3$, an order of magnitude improvement on prior work[5]. The molecules inside the junctions switch between on and off states *via* dynamic N-H bond formation due to sequential PCET resulting in a large change in the energy level alignment of the junctions and associated quantum mechanical tunneling rates. We show that this dynamical behavior leads to an unprecedented control over the device properties depending on the bias voltage sweep rate, relative humidity (RH), and pH of the environment of the junction. These dynamical features coupled to giant NDR and memory effects are interesting for new forms of matrix or logic computing[12], or neuromorphic computing[13].

Inorganic NDR devices are used in high frequency oscillators and amplifiers, and are promising alternatives for logic and memory applications in semiconductor technologies[12, 13, 14, 15], but organic devices can provide the biocompatibility or flexibility needed for healthcare or wearables[16]. Although NDR has been observed in molecular devices before[5, 6, 17], often the NDR feature visible in current density–voltage $J(V)$ curves is noisy and the underlying mechanisms are unclear and may involve filament formation[18], decomposition of the molecule[19, 20], or charge trapping at the interfaces[21, 22, 23, 24]. Stable NDR features have been only rarely reported for molecular junctions and usually require ultra-high vacuum (UHV) conditions at cryogenic temperatures (see benchmark table in Section S1 and Ref 5). For example, Perrin *et al.*[25] reported the molecular equivalent of a resonant tunnel diode with R_{PtV} ratio of 3.0–7.1 at 6 K with symmetrical shapes, and Guisinger *et al.*[20] found molecular NDR at room temperature, but with small R_{PtV} ratios <2 measured by ultrahigh vacuum scanning tunneling microscopy (STM). These examples highlight the need to develop alternative molecular switches to realize stable electronic function such as NDR in molecular junctions in ambient at room temperature[26, 27].

The mechanism of PCET depends on the physical and temporal separations of the electron and proton transfer, which in turns depends on the nuclear motions that couple them. For instance, successive initial proton (or electron) addition can accelerate the second step coupling the two processes by changing the free energy landscape of the overall reaction, or the two steps occur simultaneously (concerted PCET) involving nuclear tunneling[2, 28]. Although PCET reactions are important in many areas of chemistry, their potential in molecular devices is only starting to be explored[5, 6]. In this work, PCET stabilizes different redox states of 5,6,11,12,17,18-hexaazatrinaphthylene (H_n-HATNA

4

where n indicates the redox state) inside a molecular tunnel resulting in large hysteric switching[29]. H_n-HATNA and derivatives have been widely studied and used for applications in energy storage, photovoltaics and thin film electronics[30, 31, 32], but the mechanism of PCET in operation has not been experimentally verified. Here we report a detailed mechanistic study (by changing pH and RH and hydrogen–deuterium exchange) supported by modelling that enabled an improvement of device function of one order of magnitude highlighting the potential of PCET to advance molecular devices.

Results and Discussion

Operating principle of the dynamic molecular switch

Figure 1 shows schematic illustrations of the junctions used in this study, consisting of self-assembled monolayers (SAMs) of H_n-HATNA supported by an Au bottom electrode and contacted by a Ga_2O_3/EGaIn top electrode[5]. The full characterization of the SAMs has been reported before[5] from which we derived the molecular energy levels, and concluded that the SAMs are well-ordered and densely packed with all molecules in the upright position (see SI for brief summary). In solution, the PCET mechanism of H_n-HATNA under electrochemical conditions has been reported before and involves ring-by-ring reduction of each pyrazine ring *via* six consecutive PCET steps by dynamical N-H bond formation[29]. Although H_n-HATNA has seven different oxidation states, Fig. 1a shows only one of the on-states (for n = 1–4) and two distinct off-states (for fully oxidized (n = 0) or reduced (n = 5–6 states), for the sake of simplicity, as characterized from previously reported cyclic voltammetry (CV) experiments and density functional theory (DFT) calculations[5].

5

Figure 1b shows the operating principle of the dynamic molecular switch in terms of a simplified Gibbs free energy (ΔG) diagram and Extended Data Fig. 1 shows the corresponding energy level diagrams to explain how changes in oxidation states of H_n-HATNA modulates the current flow across the junction. The positions of the Fermi level (E_F) of the bottom and top electrodes and the molecular frontier orbitals (highest occupied molecular orbital (HOMO) and lowest unoccupied molecular orbital (LUMO)) are indicated in Extended Data Fig. 1. The applied voltage is the energy source (blue arrows in Fig. 1b) that drives changes in ΔG pushing the system continuously out of equilibrium leading to a flow of current across the molecules. Most of the electrons directly tunnel through the molecules, but occasionally an electron interaction with H_n-HATNA triggers proton transfer and N-H formation changing the molecular structure of H_n-HATNA. This change in molecular structure, in turn, leads to a change in the electronic structure of the molecule and associated energy gap between the respective on and off states (indicated by χ in Fig. 1b) and associated changes in energy level alignment (Extended Data Fig. 1). Fully oxidized H_0-HATNA has a large HOMO-LUMO gap and, therefore, the junction is in the off-state. For intermediate reduced states (n = 2, 3; Fig. 1b), H_n-HATNA turns on because a new molecular energy level appears. This midgap state changes the energy level alignment of the junction and increases the tunneling rate of the electrons (as indicated by χ in Extended Data Fig. 1). In the fully reduced form (for n = 5, 6; Fig. 1b), the midgap state disappears again restoring the large HOMO-LUMO gap that turns the junctions off. In other words, H_n-HATNA turns on and off again in a single negative voltage sweep leading to the fully reduced form (arrow labeled V^{red} in Fig. 1b) leading to NDR. By applying a positive voltage to the junction (arrow labeled V^{ox} in Fig. 1b), the H_n-HATNA

6

moieties are oxidized back to the original state (n = 0) leading to hysteretic memory behavior.

Our experiments described below show that the protons involved with PCET are provided by water from the ambient environment and that protonation precedes ET. Therefore, ET and proton coupling (PC) occur at different time scales leading to time-dependent changes in the switching probability of H_n-HATNA between the on (P_{on}) and off (P_{off}) states (indicated by solid arrows in Fig. 1b). The result is a gradual, analog change in the on and off states (in sharp contrast to the digital on/off molecular switches widely reported to-date).[5] For this reason, we introduce the term "dynamic molecular switch" to describe our junction.
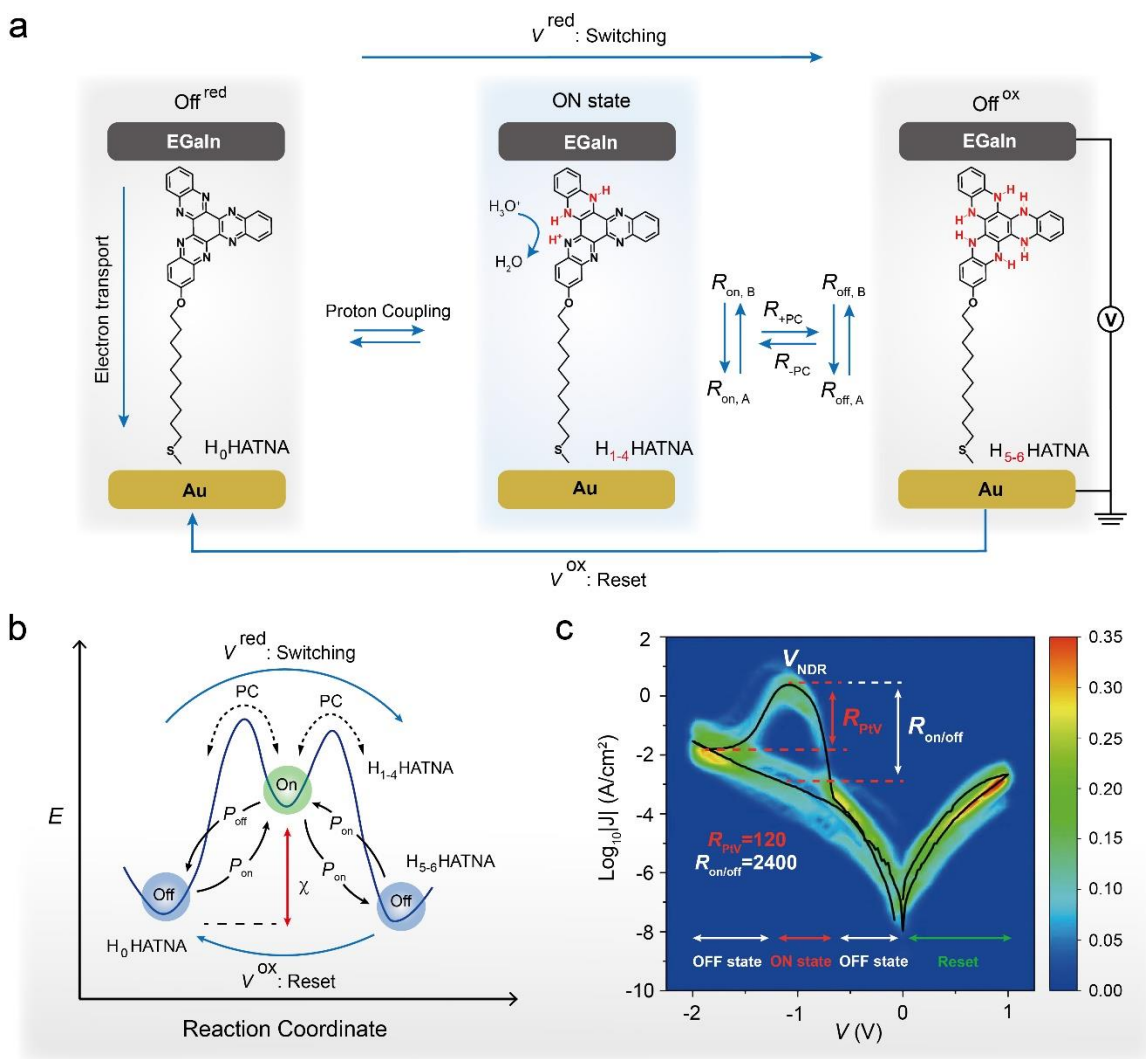
7

Fig. 1. (a) Schematic illustration of the HATNA junctions that switches between a high conductive state (on-state) and a low conductive state (off-state). (b) Operating principle of the dynamic molecular switch in terms of energy (supplied by the applied bias voltage) diagram for the PCET process. (c) Heatmap of $\log_{10}|J|$ vs. V of the Au-S-C_{10}-HATNA//Ga_2O_3/EGaIn junctions at 24 °C, relative humidity = 80%, sweep rate of 2 mV/s. The black is the median average curve of $<\log_{10}|J|>m$ vs. V with on state, off state and reset regions. In all our experiments the voltage is applied to the top electrode and the bottom electrode is grounded.

8

Theory and modeling

We used the theory developed by Migliore and Nitzan[33] to model the current–voltage I(V) curves (see Section S2 for details). This model quantifies how the switching probabilities change with time (scan rates) and we can extract the proton transfer rates as a function of relative humidity, acidity and kinetic isotope effect, as described in the following sections.

Although electron flow is coherent in nature (straight blue arrow in Fig. 1a), PC is incoherent and protons must hop over an energy barrier (dashed double black arrows in Fig. 1a). The measured J of the on (I^{on}) and off (I^{off}) states are described by the Landauer−Büttiker equation (modified to describe tunneling though SAMs[34]), where the tunneling barrier heights for the on and off states change by a value χ and the molecule–electrode coupling strength in the on and off state changes from Γ_{AB} to $\kappa\Gamma_{AB}$ (Extended Data Fig. 1). In other words, this model accounts for the lowering of the tunneling barrier by the midgap state and the associated increase in tunneling rate leading to a sharp increase in current through the multiplication factor κ and the value χ which was estimated from DFT[5]. The much slower proton hopping rates (R_{PC}) are described by Marcus theory[21] (which is often used to describe PC steps[2, 11, 35]) leading to a time-dependent switching probability (see Section S2 for full expressions). Thus, the current that flows across the junction depends on the probability P to be in the on and off states where $P^{on}(V) = 1 - P^{\overline{off}}(V)$ and is given by

$$I(V) = P^{on}(V)I^{on}(V) + P^{\overline{off}}(V)I^{\overline{off}}(V) \qquad (Eqn 1)$$

The switching probability depends on the R_{+PC} and R_{-PC} giving the junctions their time-dependent character as follows:

9

$$\frac{\mathrm{d}P^{on}}{\mathrm{d}t} = (1 - P^{on}) < R_{+PC} > -P^{on} < R_{-PC} > \qquad (Eqn 2)$$

Giant negative differential resistance (NDR)

Fig. 1c shows the measured heatmap of the J(V) response from the HATNA junctions (see Methods for details). The large hysteric NDR peak at negative bias is caused by the switching of the molecules from the off, to the on, and to the off state again (as visualized in Fig. 1a in the direction of V^{red}). In our experiments, the voltage was first increased from 0 V to +1.0 V to ensure n = 0. As the bias is then dialed back and into negative voltage, the current increases sharply at around -0.9 V because the midgap state enters the bias window[5]. Further increasing the voltage results in continuous reduction of HATNA which then turns off again for n = 5, 6 leading to a decrease of current despite an increase of voltage, *i.e.*, NDR. The HATNA moieties remain in reduced form when the voltage changes from -2 V to 0 V resulting in large hysteretic behavior. The reduced H_n-HATNA moieties can oxidize back to HATNA (n = 0) only at positive bias.

The individual J(V) traces in Fig. 1c are smooth and the NDR peak is symmetrical and stable in our molecular devices. These features indicate that our switches avoid stochastic transitions characterized by excessive noise, or triangular peak shapes, as frequently observed[21, 22, 33, 36, 37] which cannot be modelled with any tunneling model and strongly indicate filament formation[38] (Section S1). Unlike resonant tunneling diodes[17], our junctions show pronounced hysteresis which is a desirable feature for device applications, *e.g.*, memory or artificial neurons[39, 40]. Fig. 1c defines the NDR peak position (V_{NDR}), peak-to-valley ratio (R_{PtV}), and current on/off ratio ($R_{on/off}$, current at forward bias divided by current at reverse bias at $V = V_{NDR}$). The value of R_{PtV} and $R_{on/off}$ are 120 ± 6.6

10

and $(2.4 \pm 0.6) \times 10^3$ at a scan rate of 2 mV/s, and the value of R_{PtV} is comparable to state-of-the-art molecular resonant tunnel diodes[17]. To our knowledge, giant hysteric NDR with such a large $R_{on/off}$ has not been reported before (see benchmarks in Section S1 and Ref 5).

Environmental control over NDR

It is well-known that PCET is highly sensitive to water[2, 41, 42, 43]. To investigate the mechanism of NDR in more detail and to further assess the importance of PCET in driving NDR, we conducted the J(V) measurements at 10 mV/s in a controlled atmosphere of Ar with a relative humidity RH ranging from 5% to 85% (water condensation hampered experiments at RH > 85%; Section S1.5.2[44]). Figure 2a-c shows the heatmaps of all $\log_{10}|J|$ *vs.* V curves of the junctions measured at RH of 30%, 60% and 80%, respectively. In each heatmap, the black line represents the log-median average curve ($<\log_{10}|J|>_m$ *vs.* V). Figure 2d (and see also Table S2) shows that NDR was absent at RH = 5%, and that the value of R_{PtV} increases from 1.2 ± 0.1 at RH = 10% to 41.1 ± 6.7 at RH = 85% (error is the mean absolute deviation). Figure 2e shows the $<\log_{10}|J|>_m$ *vs.* V curves as a function of RH along with a clear NDR peak shift at RH = 40–50% as indicated by the dashed line. These results demonstrate that ambient water is important in the mechanism of charge transport and that it is the proton source for PCET in our junctions.

It is well-known that water adsorption on surfaces (or interfacial water) can lead to changes in the energy level alignment of surfaces[45, 46]. We note that there is a distinct, abrupt shift in the NDR peak position (V_{NDR} defined in Fig. 1c) at RH = 40–50% of about 260 meV (as indicated by the vertical dashed lines, Fig. 2e). This shift suggests that water causes a small change in energy-level alignment of the junctions at around this humidity

11

level. To investigate this effect in more detail, we conducted Kelvin probe force microscopy (KPFM) experiments at different RH levels (Section S1.6). These measurements reveal a small change in the work function of the gold substrate of around 40–50 meV at higher RH, supporting the hypothesis that the shift in V_{NDR} is caused by water adsorption.
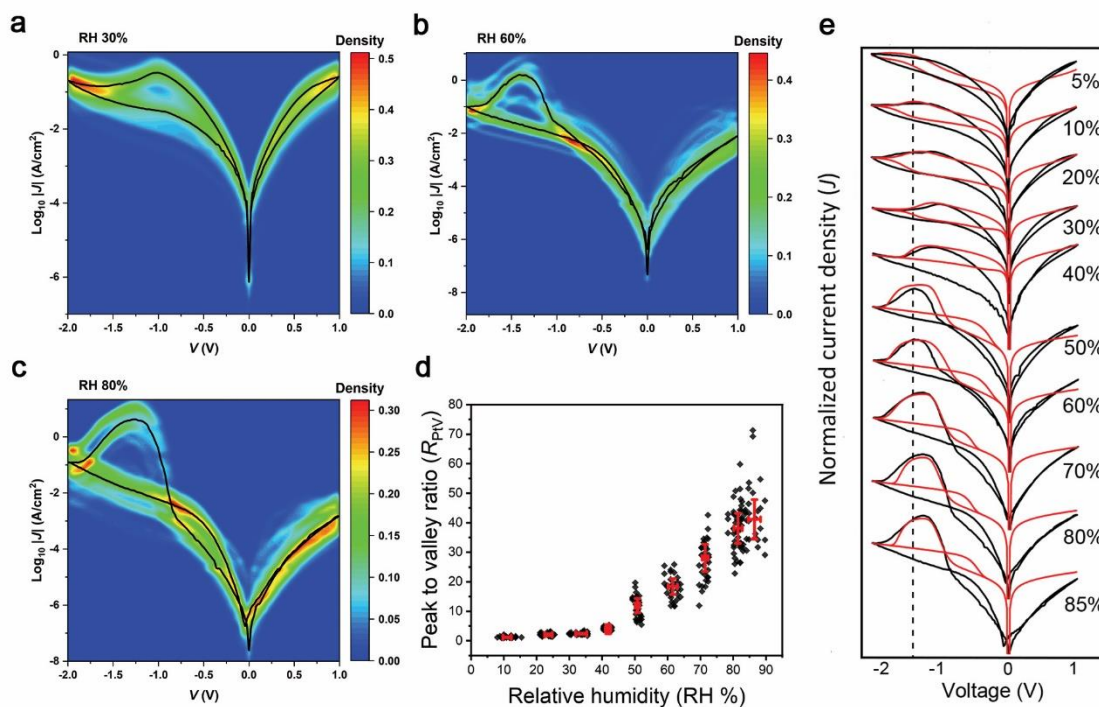

Fig. 2. (a) $Log_{10}|J|$ *vs.* V heatmap of the Au^{TS}-SC_{10}-HATNA//EGaIn junctions at RH = 30%, (b) RH = 60%, and (c) RH = 80%. The black line is the mean $<log_{10}|J|>_m$ *vs.* V curve. (d) Distribution of R_{PtV} as a function of RH for all measured junctions. The error bars represent the standard deviations of the mean value of R_{PtV}. (e) Typical J-V curves of the junction with RH increasing from 5 to 85%. All measurements were conducted at 10 mV/s. The dashed line intersecting the NDR peak is a visual guide. The red curves are the modelling fits to the data.

12

Figure 2e shows a direct comparison between experimental and theoretical J(V) curves (black and red lines) as a function of humidity. The model reproduces the experimental results in detail accounting for the gradual change in shape of the J(V) curves and the eventual disappearance of the NDR peak at low relative humidity values. While all parameters from the fits are given in Table S5, analysis of these fits determined that much of the variation in responses from low humidity to high humidity can be explained by just two parameters, κ and λ, that govern the J(V) response. As mentioned above, κ (≥ 1) is a multiplier describing the change in the coupling strength of the molecule to the electrodes between the on (Γ_{AB}) and off ($\kappa\Gamma_{AB}$) states with $\kappa = 1$ representing the case where no change in the coupling strength occurs. Extended Data Fig. 2a shows how κ changes as a function of RH. At low RH, $\kappa \sim 1$ showing no noticeable change in the molecule–electrode coupling strength, but we find a large increase to $\kappa \sim 10$ for high RH values, indicating a large increase in coupling strength when more water is present. The other governing parameter, λ, represents the reorganization energy in the junction as PCET progresses. Extended Data Fig. 2b shows a decrease in the value for λ as the RH is increased, clearly illustrating how the protonation process is facilitated at higher RH values.

Mechanism of proton-coupled electron transfer (PCET)

There are in principle three types of PCET reactions where the H^+ and e^- transfer simultaneously, or sequentially where either H^+ or e^- precedes the addition of the other charge carrier. Ohsaka et al.[29] suggested that initial protonation of HATNA precedes PCET under wet electrochemical conditions in acidic electrolyte. To establish whether initial protonation is important in our junctions, we carried out the following experiments. By

13

flowing Ar though 1 M aqueous HCl or 1.3 M aqueous NH_4OH, we obtained an acidic or basic atmosphere with RH = 60%. Although it is not possible to measure the pH of molecular junctions directly, the effect of the acidity of the atmosphere on the junction characteristics was significant. Figure 3 shows the heatmaps of the J(V) curves along with the $<\log_{10}|J|>_m$ *vs.* V curves recorded in acidic, basic or neutral Ar atmospheres with RH = 62–65%. Under neutral conditions, $R_{PtV} = 18.5 \pm 2.8$, but its value increases to 31.2 ± 3.2 under acidic conditions while NDR is suppressed under basic conditions and R_{PtV} decreases to 7.9 ± 1.4. The values of $R_{on/off}$ under acidic, basic and neutral conditions are 198 ± 23, 178 ± 95 and 104 ± 21, respectively. Figure 5e shows a direct comparison between experimental and theoretical I(V) curves (black and red lines) as a function of pH. The value of κ decreases sharply from acidic to basic conditions while λ is far less sensitive (Extended Data Fig. 2). We repeated the measurement under D_2O atmosphere to determine the kinetic isotope effect (KIE). Figure 3c shows the heatmap of the junction recorded under D_2O atmosphere with RH = 63%. The value of R_{PtV} decreases to 11.4 ± 2.2 with respect to that recorded under H_2O atmosphere resulting in a H/D ratio of 1.6. Fitting to theory shows that this change is mainly driven by a decrease of κ (Extended Data Fig. 2). These observations are consistent with stepwise PCET reaction where a proton first binds to HATNA, which may be favored by the basic nature of HATNA, followed by electron addition and N-H bond formation[3, 28]. Figure 3d summarizes the distribution of the value of R_{PtV} obtained from the junctions under different conditions with the corresponding $<\log_{10}|J|>_m$ *vs.* V curves in Figure 3e. These results show that it is possible to control the NDR effect by changing the concentration of H^+ to gate the tunneling channels in the on and off states.
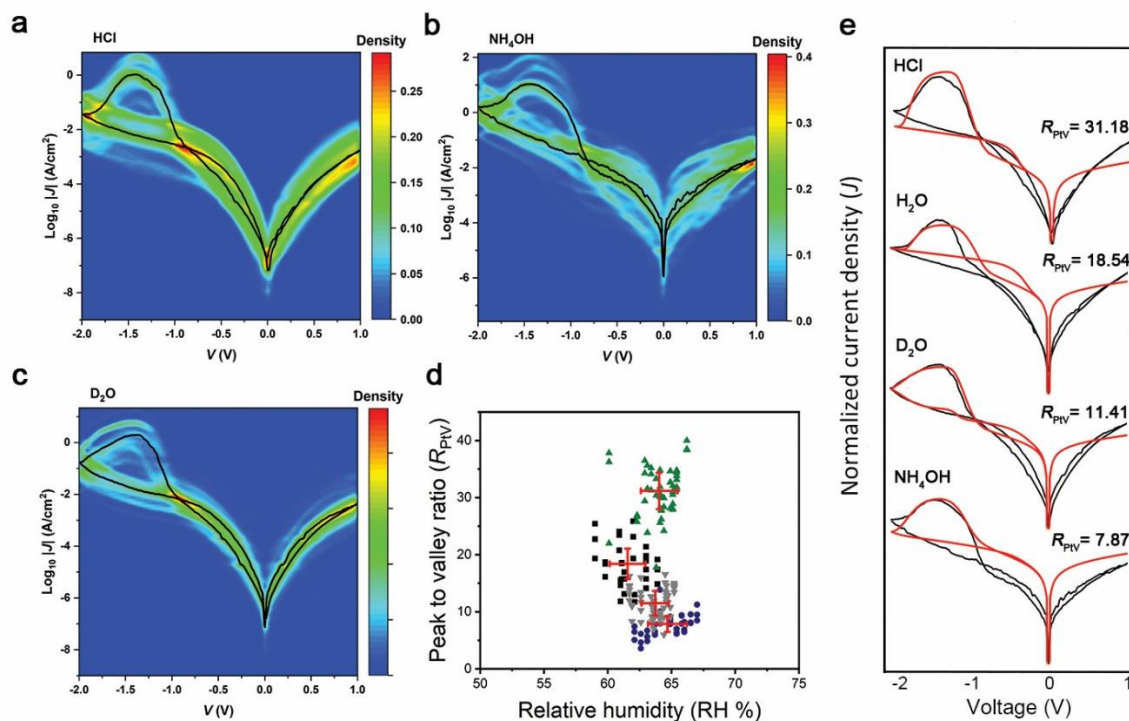
14

Fig. 3. (a) $Log_{10}|J|$ *vs.* V heatmap of the Au^{TS}-SC_{10}-HATNA//EGaIn junctions under the condition of HCl, NH_4OH (b) and D_2O (c) at RH 60%, the black line is $<log_{10}|J|>_m$ *vs.* V curve. (d) The distribution of R_{PtV} as a function of the determined conditions under basic (blue), acidic (green), D_2O (grey) and neutral atmospheres (black), along with (e) the corresponding log-average J-V curves of the junction with red curves showing the modeling fits to the measured data.

Dynamical switching behavior

To demonstrate the dynamic behavior of the junctions, we recorded $J(V)$ curves at scan rates ranging from 0 to 250 mV/s. Fig. 4a and Fig. 4b show the data in the corresponding semi-log plots and linear scales. First, the R_{PtV} ratio decreased from 18.8 at 10 mV/s to 1.17 at 250 mV/s while the NDR peak current increases from 142 μA at 10 mV/s to 254 μA at 36 mV/s and decreases to 72 μA at 250 mV/s (Extended Data Fig. 3).

15

This dynamical behavior is also clearly reflected in the changes in the value of ΔI_{NDR} at forward I_{fw} and backward bias I_{bwd} direction ($\Delta I = I_{\text{fwd}} - I_{\text{bwd}}$) which goes through a maximum at 36 mV/s (Fig. 4d). To establish the dynamical behavior of the junctions, we mapped the changes in switching probabilities of the molecules inside the junctions by fitting our data to the model by Nitzan[33]. The agreement between experiment and theory is excellent (see Section S2 for details of fitting) and the experimentally measured dynamical nature of the system is consistent with the behavior predicted by the Nitzan model.

Fig. 4c shows the evolution of the probability of the junction to be in the off state ($P^{\overline{AB}}$) as bias voltage cycles ($0 \rightarrow +1$ V [1] $\rightarrow 0$ V [2] $\rightarrow -2$V [3] $\rightarrow 0$V [4]) are repeated with different scan rates. Starting in the on-state (1 and 2) with $P^{\overline{AB}} = 0$ (blue line), the system evolves towards the off state (3) and completely turns off (4) and then shifts back towards the on state at positive bias of the second bias voltage cycle (1 and 2 of the red line) at low scan rates. However, at increasingly high scan rates, the system only partially recovers to the on state at positive bias because the system does not have sufficient time to switch back. Hence, $P^{\overline{AB}}$ increases as the cycling evolves, with each initial probability at the start of the cycle progressively approaching $P^{\overline{AB}} = 1$. One would expect that ΔI decreases in pace with $P^{\overline{AB}}$, but we find that ΔI reaches a maximum around 25–36 mV/s (Fig. 4d, e), due to displacement of the transition to high negative voltages as scan rate increases, which affects current (larger at higher voltage). Therefore, ΔI is a trade-off between the initial probability and the scan rate which together determine when NDR can be observed.
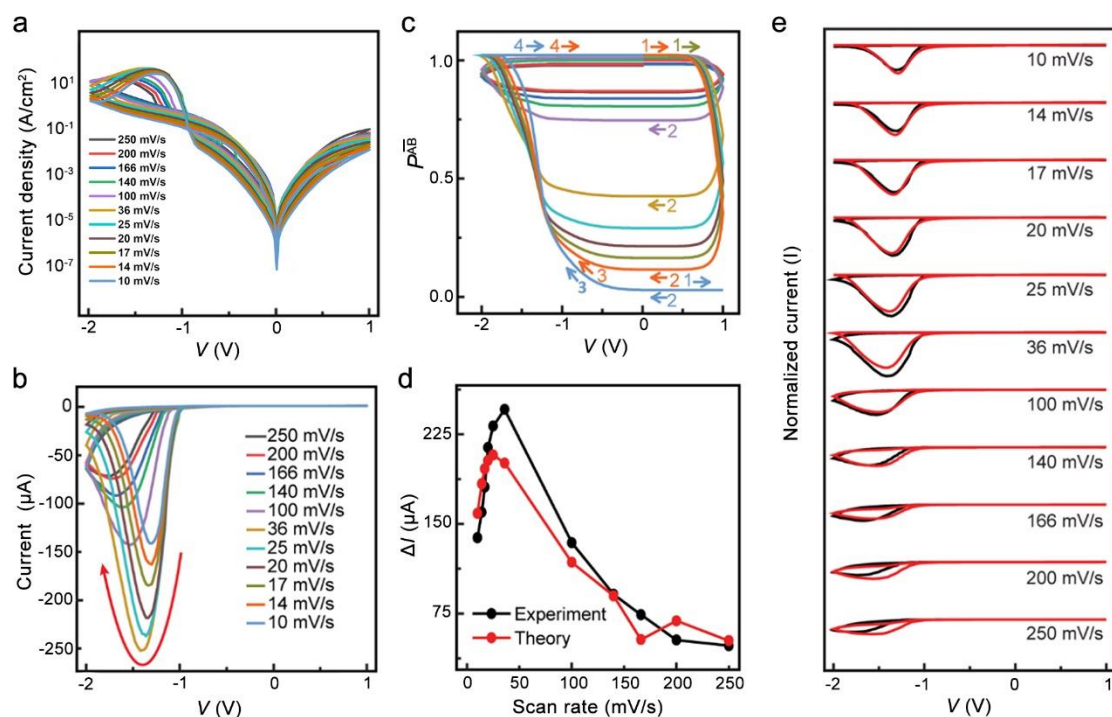
16

Fig. 4. Sweep rate characterization of the junctions. (a, b) Scan rate dependent J(V) and I(V) measurements. **(c)** Calculated probability of the system being in the off state ($P^{\overline{AB}}$) at the different scan rates given in panel b, with labels 1-4 marking bias voltage cycles $0 \rightarrow +1V$ [1] $\rightarrow 0V$ [2] $\rightarrow -2V$ [3] $\rightarrow 0V$ [4]. **(d)** ΔI values ($\Delta I = I_{fwd} - I_{bwd}$) between the forward ($I_{fwd}$) and backward ($I_{bwd}$) sweeps at V_{NDR} determined from **(e)** the I(V) fits (red) to the experimental I(V) data (black).

Conclusions

In summary, we report giant NDR of $R_{PtV} = 120 \pm 6.6$ enabled by PCET via optimization of pH, humidity and scan rate. The NDR feature in our junctions is stable and is not disadvantaged by the stochastic behavior found in NDR devices based on charge traps or filament formation[19, 22, 23, 24], because the different oxidation states of the HATNA active layer are stabilized by reversible covalent N-H bonds. The molecules switch depending on

17

the bias polarity resulting in hysteresis with large values of current on/off ratios of $(2.4\pm 0.6)\times 10^3$. This combined functionality of an on/off switch and NDR provides a pathway to develop new types of devices beyond resonant tunneling diodes. The NDR modulation by humidity, pH and sweep rate could be a useful new feature for next-generation sensors and artificial neural networks that respond to, and learn from their environment[5, 6, 47, 48, 49]. Our findings demonstrate that PCET is an advantageous mechanism of charge transport in molecular devices, enabling improved performance and generating new types of dynamical electronic function for molecular-scale electronics applications.

References

1. Choi GJ, Zhu Q, Miller DC, Gu CJ, Knowles RR. Catalytic alkylation of remote C–H bonds enabled by proton-coupled electron transfer. *Nature* 2016, **539**(7628)**:** 268-271.

2. Migliore A, Polizzi NF, Therien MJ, Beratan DN. Biochemistry and Theory of Proton-Coupled Electron Transfer. *Chem Rev* 2014, **114**(7)**:** 3381-3465.

3. Weinberg DR, Gagliardi CJ, Hull JF, Murphy CF, Kent CA, Westlake BC*, et al.* Proton-Coupled Electron Transfer. *Chem Rev* 2012, **112**(7)**:** 4016-4093.

4. Nocera DG. The Artificial Leaf. *Acc Chem Res* 2012, **45**(5)**:** 767-776.

5. Wang Y, Zhang Q, Astier HPAG, Nickle C, Soni S, Alami FA*, et al.* Dynamic molecular switches with hysteretic negative differential conductance emulating synaptic behaviour. *Nat Mater* 2022, **21**(12)**:** 1403-1411.

6. Wang Z, Li Z, Li C, Ji X, Song X, Yu X, *et al.* Generic dynamic molecular devices by quantitative non-steady-state proton/water-coupled electron transport kinetics. *Proc Natl Acad Sci* 2023, **120**(24)**:** e2304506120.

7. Gehring P, Thijssen JM, van der Zant HSJ. Single-molecule quantum-transport phenomena in break junctions. *Nat Rev Phys* 2019, **1**(6)**:** 381-396.

8. Wang M, Wang T, Ojambati OS, Duffin TJ, Kang K, Lee T, *et al.* Plasmonic phenomena in molecular junctions: principles and applications. *Nat Rev Chem* 2022, **6**(10)**:** 681-704.

9. Xin N, Guan J, Zhou C, Chen X, Gu C, Li Y, *et al.* Concepts in the design and engineering of single-molecule electronic devices. *Nat Rev Phys* 2019, **1**(3)**:** 211-230.

10. Parada GA, Goldsmith ZK, Kolmar S, Pettersson Rimgard B, Mercado BQ, Hammarström L, *et al.* Concerted proton-electron transfer reactions in the Marcus inverted region. *Science* 2019, **364**(6439)**:** 471-475.

11. Mayer JM. Understanding Hydrogen Atom Transfer: From Bond Strengths to Marcus Theory. *Acc Chem Res* 2011, **44**(1)**:** 36-46.

12. Kim K-H, Park H-Y, Shim J, Shin G, Andreev M, Koo J, *et al.* A multiple negative differential resistance heterojunction device and its circuit application to ternary static random access memory. *Nanoscale Horiz* 2020, **5**(4)**:** 654-662.

13. Seo S, Koo J, Choi J-W, Heo K, Andreev M, Lee J-J, *et al.* Controllable potential barrier for multiple negative-differential-transconductance and its application to multi-valued logic computing. *npj 2D Mater Appl* 2021, **5**(1)**:** 32.

19

14.   Gherabli R, Zektzer R, Grajower M, Shappir J, Frydendahl C, Levy U. CMOS-compatible electro-optical SRAM cavity device based on negative differential resistance. *Sci Adv 2023*, **9**(15)**:** eadf5589.

15.   Seo S, Cho J-I, Jung K-S, Andreev M, Lee J-H, Ahn H*, et al.* A Van Der Waals Reconfigurable Multi-Valued Logic Device and Circuit Based on Tunable Negative-Differential-Resistance Phenomenon. *Adv Mater* 2022, **34**(36)**:** 2202799.

16.   Kaushal JB, Raut P, Kumar S. Organic Electronics in Biosensing: A Promising Frontier for Medical and Environmental Applications. *Biosensors* 2023, **13**(11)**:** 976.

17.   Perrin ML, Frisenda R, Koole M, Seldenthuis JS, Gil JAC, Valkenier H*, et al.* Large negative differential conductance in single-molecule break junctions. *Nat Nanotechnol* 2014, **9**(10)**:** 830-834.

18.   Stadler P, Hesser G, Fromherz T, Matt GJ, Neugebauer H, Sariciftci SN. Current filamentation and negative differential resistance in C60 diodes. *physica status solidi (b)* 2008, **245**(10)**:** 2300-2302.

19.   He J, Lindsay SM. On the Mechanism of Negative Differential Resistance in Ferrocenylundecanethiol Self-Assembled Monolayers. *J Am Chem Soc* 2005, **127**(34)**:** 11932-11933.

20.   Guisinger NP, Greene ME, Basu R, Baluch AS, Hersam MC. Room Temperature Negative Differential Resistance through Individual Organic Molecules on Silicon Surfaces. *Nano Lett* 2004, **4**(1)**:** 55-59.

21.   Xu B, Dubi Y. Negative differential conductance in molecular junctions: an overview of experiment and theory. *J Phys: Condens Matter* 2015, **27**(26)**:** 263202.

22.   Fung ED, Gelbwaser D, Taylor J, Low J, Xia J, Davydenko I*, et al.* Breaking down resonance: nonlinear transport and the breakdown of coherent tunneling models in single molecule junctions. *Nano Lett* 2019, **19**(4)**:** 2555-2561.

23.   Song Y, Jeong H, Jang J, Kim T-Y, Yoo D, Kim Y*, et al.* 1/f Noise Scaling Analysis in Unipolar-Type Organic Nanocomposite Resistive Memory. *ACS Nano* 2015, **9**(7)**:** 7697-7703.

24.   Song Y, Jeong H, Chung S, Ahn GH, Kim T-Y, Jang J*, et al.* Origin of multi-level switching and telegraphic noise in organic nanocomposite memory devices. *Sci Rep* 2016, **6**(1)**:** 33967.

25.   Perrin ML, Frisenda R, Koole M, Seldenthuis JS, Gil JAC, Valkenier H*, et al.* Large negative differential conductance in single-molecule break junctions. *Nat Nanotechnol* 2014, **9:** 830-834.

26.   Albo A, Hu Q, Reno JL. Room temperature negative differential resistance in terahertz quantum cascade laser structures. *Appl Phys Lett* 2016, **109**(8).

27.   Chang W-H, Lu C-I, Yang TH, Yang S-T, Simbulan KB, Lin C-P*, et al.* Defect-engineered room temperature negative differential resistance in monolayer MoS2 transistors. *Nanoscale Horiz* 2022, **7**(12)**:** 1533-1539.

28.   Tyburski R, Liu T, Glover SD, Hammarström L. Proton-Coupled Electron Transfer Guidelines, Fair and Square. *J Am Chem Soc* 2021, **143**(2)**:** 560-576.

29. Wang R, Okajima T, Kitamura F, Matsumoto N, Thiemann T, Mataka S*, et al.* Cyclic and Normal Pulse Voltammetric Studies of 2,3,6,7,10,11-Hexaphenylhexazatriphenylene Using a Benzonitrile Thin Layer-Coated Glassy Carbon Electrode. *J Phys Chem B* 2003, **107**(35)**:** 9452-9458.

30. Segura JL, Juárez R, Ramos M, Seoane C. Hexaazatriphenylene (HAT) derivatives: from synthesis to molecular design, self-organization and device applications. *Chem Soc Rev* 2015, **44**(19)**:** 6850-6885.

31. Tian Z, López-Salas N, Liu C, Liu T, Antonietti M. C_2N: A Class of Covalent Frameworks with Unique Properties. *Adv Sci* 2020, **7**(24)**:** 2001767.

32. Peng C, Ning G-H, Su J, Zhong G, Tang W, Tian B*, et al.* Reversible multi-electron redox chemistry of π-conjugated N-containing heteroaromatic molecule-based organic cathodes. *Nat Energy* 2017, **2**(7)**:** 17074.

33. Migliore A, Nitzan A. Irreversibility and Hysteresis in Redox Molecular Conduction Junctions. *J Am Chem Soc* 2013, **135**(25)**:** 9420-9432.

34. Garrigues AR, Yuan L, Wang L, Mucciolo ER, Thompon D, del Barco E*, et al.* A Single-Level Tunnel Model to Account for Electrical Transport through Single Molecule- and Self-Assembled Monolayer-based Junctions. *Sci Rep* 2016, **6**(1)**:** 26517.

35. Warren JJ, Mayer JM. Chapter 1 Application of the Marcus Cross Relation to Hydrogen Atom Transfer/Proton-Coupled Electron Transfer Reactions. *Proton-Coupled Electron Transfer: A Carrefour of Chemical Reactivity Traditions*. The Royal Society of Chemistry, 2012, pp 1-31.

22

36. Jia C, Migliore A, Xin N, Huang S, Wang J, Yang Q, *et al.* Covalently bonded single-molecule junctions with stable and reversible photoswitched conductivity. *Science* 2016, **352**(6292): 1443-1445.

37. Schwarz F, Kastlunger G, Lissel F, Egler-Lucas C, Semenov SN, Venkatesan K, *et al.* Field-induced conductance switching by charge-state alternation in organometallic single-molecule junctions. *Nat Nanotechnol* 2016, **11**(2): 170-176.

38. Chen J, Reed MA, Rawlett AM, Tour JM. Large On-Off Ratios and Negative Differential Resistance in a Molecular Electronic Device. *Science* 1999, **286**(5444): 1550-1552.

39. Kumar S, Strachan JP, Williams RS. Chaotic dynamics in nanoscale NbO_2 Mott memristors for analogue computing. *Nature* 2017, **548**(7667): 318-321.

40. Kumar S, Williams RS, Wang Z. Third-order nanocircuit elements for neuromorphic engineering. *Nature* 2020, **585**(7826): 518-523.

41. Zhong J, Reinhardt CR, Hammes-Schiffer S. Role of Water in Proton-Coupled Electron Transfer between Tyrosine and Cysteine in Ribonucleotide Reductase. *J Am Chem Soc* 2022, **144**(16): 7208-7214.

42. Sharma V, Enkavi G, Vattulainen I, Róg T, Wikström M. Proton-coupled electron transfer and the role of water molecules in proton pumping by cytochrome c oxidase. *Proc Natl Acad Sci* 2015, **112**(7): 2040-2045.

43. Song M-K, Namgung SD, Choi D, Kim H, Seo H, Ju M, *et al.* Proton-enabled activation of peptide materials for biological bimodal memory. *Nat Commun* 2020, **11**(1): 5896.

44. Barber JR, Yoon HJ, Bowers CM, Thuo MM, Breiten B, Gooding DM, *et al.* Influence of Environment on the Measurement of Rates of Charge Transport across Ag^{TS}/SAM//Ga$_2$O$_3$/EGaIn Junctions. *Chem Mater* 2014, **26**(13)**:** 3938-3947.

45. Gonella G, Backus EHG, Nagata Y, Bonthuis DJ, Loche P, Schlaich A, *et al.* Water at charged interfaces. *Nat Rev Chem* 2021, **5**(7)**:** 466-485.

46. White JJ, Hinsch JJ, Bennett WW, Wang Y. Theoretical understanding of water adsorption on stepped iron surfaces. *Appl Surf Sci* 2022, **605:** 154650.

47. Sangwan VK, Hersam MC. Neuromorphic nanoelectronic materials. *Nat Nanotechnol* 2020, **15**(7)**:** 517-528.

48. Wang T, Meng J, Zhou X, Liu Y, He Z, Han Q, *et al.* Reconfigurable neuromorphic memristor network for ultralow-power smart textile electronics. *Nat Commun* 2022, **13**(1)**:** 7432.

49. Li Y, Artés JM, Demir B, Gokce S, Mohammad HM, Alangari M, *et al.* Detection and identification of genetic material via single-molecule conductance. *Nat Nanotechnol* 2018, **13**(12)**:** 1167-1173.

Methods

Molecule synthesis and self-assembled monolayer (SAM) formation. 5,6,11,12,17,18-hexaazatrinaphthylene (HATNA) was synthesized and characterized in accordance with our previous report[5] and the HATNA SAMs were prepared by employing a well-established method[50]. 1.0 mg HS-C$_{10}$-HATNA was dissolved in 5 ml of freshly distilled tetrahydrofuran (THF) at a concentration of 0.35 M. The solution was then given a 15 min N$_2$ flush to eliminate the oxygen. Subsequently, freshly prepared Au surfaces were immersed in the solution. After about 24 h, the Au substrates were removed from the solution, promptly washed with THF and ethanol, and gently dried in a flow of N$_2$. For Kelvin probe force microscopy (KPFM) experiments HATNA-SAc SAMs were employed. 1.0 mg AcS-C$_{10}$-HATNA was dissolved in 5 ml of freshly distilled tetrahydrofuran (THF) at a concentration of 0.33 M. This was following by addition of 20μl ammonia (26-28%), and freshly prepared Au surfaces were immersed in the solution. After about 24 h, the Au substrates were removed from the solution and immediately washed with large volumes of THF and ethanol, and the substrates were then gently dried with N$_2$[50].

Electrode preparation. The top electrode was prepared based on the well-known EGaIn technique. In this procedure, an EGaIn alloy was ultilized to shape a conical tip, which was subsequently used for establishing contacts with the SAMs as described in detail in previous publications[51]. The well-known template-stripping method was used to fabricate the bottom electrode[52]. Initially, a 200 nm thick Au (99.999% Au granules, ACI Alloys) was thermally evaporated onto a silicon wafer (featuring a native SiO$_2$ thin layer on the surface, Syst Integration Pte Ltd). Pre-cleaned glass slides were then glued on the Au

25

surface using thermal glue (EPOTEK 353ND). The Au thin film was then heated at 80 °C for 3 h to cure the adhesive. The resulting Au electrode was stored in a dry box and template-stripped immediately prior to usage.

Surface characterization. The X-ray photoelectron spectroscopy (XPS), ultraviolet photoelectron spectroscopy (UPS), and near-edge X-ray absorption fine structure (NEXAFS) spectroscopy of the HATNA SAMs were conducted on template-stripped Au surfaces coated with S-C$_{10}$-HATNA SAM, using previously described procedures[5, 53].

Junction fabrication and electrical measurements in air. The junctions were fabricated with a grounded Au bottom electrode, a HATNA monolayer, and a cone-shaped GaOx/EGaIn top electrode, where the bias was applied to the top EGaIn electrode, following the method given in ref [51]. Electrical measurements were conducted by employing a LabVIEW-controlled Keithley 6430 source meter. J(V) curves were recorded with a voltage sweep sequence from 0 V→ +1 V → 0 V → -2 V → 0 V, at intervals of 20 mV.

Junction fabrication and electrical measurements in different RH and pH. Here, we report a modified setup of the EGaIn technique with atmospheric control of the junction to probe the electrical properties and explore the underlying mechanism of NDR effects in large area junctions. The detailed experimental setup and atmospheric control of humidity level and acid/base conditions can be found in the SI (Supplementary Section S1.2).

The Kelvin probe force microscopy (KPFM). The experiments were conducted in a Bruker Icon atomic force microscopy (AFM) in a controlled temperature and humidity environment. The humidity is controlled by a home-build humidity controller which mixes N_2 gas with H_2O vapor[54]. The humidity is measured (with a TFA®Digital Professional Thermo-Hygrometer KLIMA BEE) both at the inlet and the outlet of the environmental chamber, to verify if the relative humidity remains constant throughout the process. The sample is heated using a platinum resistive-type heater in a ceramic body and a tungsten cap controlled by a thermal applications controller. Before the measurement, the sample is first heated to 90ºC in a N_2 environment to remove any water present in the system. A heavily doped n-type Si-cantilever with a resonance frequency 75 kHz and a force constant of 2.8 N/m (SSS-FMR, Nanosensors). The FM-KPFM mode is used, where the electrostatic force gradient is detected by the frequency shift of the cantilever oscillation. The tip work function is determined to be 4.5 eV after calibration on a Au surface. The sample was grounded in the KPFM-measurement and therefore the contact potential difference (V_{CPD}) is determined by:

$$V_{CPD} = \frac{\varphi_t + \varphi_s}{|e|}$$

With e the elementary charge and φ_s and φ_t the work function of the sample and tip, respectively. When the work function of the tip is known, the work function of the sample can be determined.

Statistical analysis of J(V) characteristics. We performed the statistical analysis of J(V) data with the median averages of the current ($<\log_{10}|J|>_m$) and the median absolute deviations (σ_m) following a previously reported method[55]. This approach is applied for its

27

independence from presumptions about the data distribution as detailed elucidated in ref[5]. The values of $<\log_{10}|J|>_m$ and σ_m were calculated from the $\log_{10}|J|$ values measured at each bias step. To visualize the $J(V)$ curves, heatmaps were generated using OriginPro 2019b software with 2D kernel density estimations. In these estimations, the density values were calculated based on a bi-dimensional Gaussian kernel, and the bandwidth was determined through a bivariate kernel density estimator with a grid size of 100.

Theoretical Modelling of the Transport Dynamics. We analyzed the switching behavior of the junctions using a theoretical model developed by Migliore and Nitzan[33]. The currents passing through the junctions in the on and off conduction states were described by the standard Landauer single-level quantum model, adjusted to describe currents across large-area junctions[34]. The fitting results are given in Fig. 2-4. The detailed description of the modelling is provided in Supplementary Section S2.

Data availability: Data and codes are available in the supplementary materials and at https://dataverse.harvard.edu/privateurl.xhtml?token=6f7a9d86-b051-4a2b-8306-45028373aa43.

References

50.   Singh A, Dahanayaka DH, Biswas A, Bumm LA, Halterman RL. Molecularly Ordered Decanethiolate Self-Assembled Monolayers on Au(111) from in Situ Cleaved Decanethioacetate: An NMR and STM Study of the Efficacy of Reagents for Thioacetate Cleavage. *Langmuir* 2010, **26**(16): 13221-13226.

51. Chen X, Roemer M, Yuan L, Du W, Thompson D, del Barco E, et al. Molecular diodes with rectification ratios exceeding 105 driven by electrostatic interactions. *Nat Nanotechnol* 2017, **12**(8): 797-803.

52. Yuan L, Jiang L, Thompson D, Nijhuis CA. On the Remarkable Role of Surface Topography of the Bottom Electrodes in Blocking Leakage Currents in Molecular Diodes. *J Am Chem Soc* 2014, **136**(18): 6554-6557.

53. Yuan L, Breuer R, Jiang L, Schmittel M, Nijhuis CA. A Molecular Diode with a Statistically Robust Rectification Ratio of Three Orders of Magnitude. *Nano Lett* 2015, **15**(8): 5506-5512.

54. Jimidar ISM, Kwiecinski W, Roozendaal G, Kooij ES, Gardeniers HJGE, Desmet G, et al. Influence of Wettability and Geometry on Contact Electrification between Nonionic Insulators. *ACS Appl. Mater. Interfaces* 2023, **15**(35): 42004-42014.

55. Reus WF, Nijhuis CA, Barber JR, Thuo MM, Tricard S, Whitesides GM. Statistical Tools for Analyzing Measurements of Charge Transport. *J Phys Chem C* 2012, **116**(11): 6714-6733.

ACKNOWLEDGEMENTS

Author contributions

C.A.N. conceived and supervised the project. E.d.B. and C.N. conducted all the numerical modelling. Y.W. synthesized the compounds. Z.Z. performed the AR-XPS and NEXAFS measurements and analyzed, with the assistance of D.Q, the data. Q.Z. and Y.W. performed the electrical measurements. A.L. developed the Origin code for electrical data analysis. C.A.N., E.d.B. and D.T. wrote the manuscript and all authors commented on it.

Competing interests: The authors declare no competing interests.
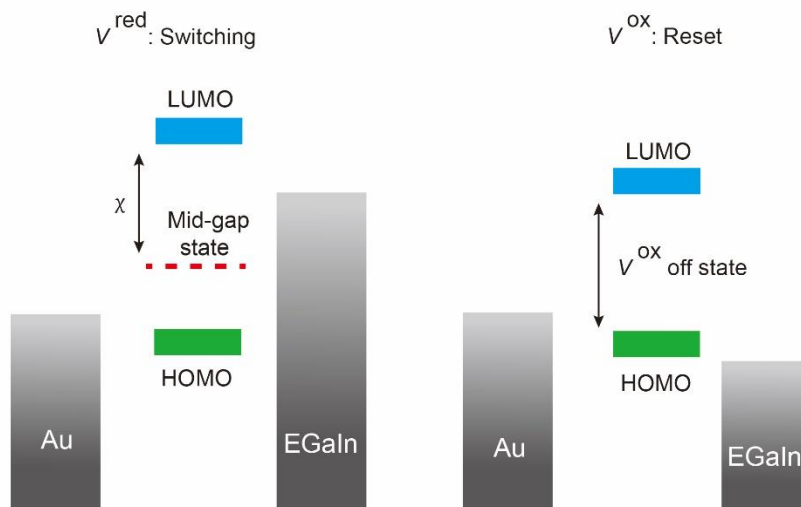
Additional information

Extended data is available for this paper at https://doi.org/xxx.

Supplementary information is available for this paper at https://doi.org/xxx.

Correspondence and requests for materials should be addressed to E.d.B., D.T. or C.A.N.

Reprints and permissions information is available at www.nature.com/reprints.
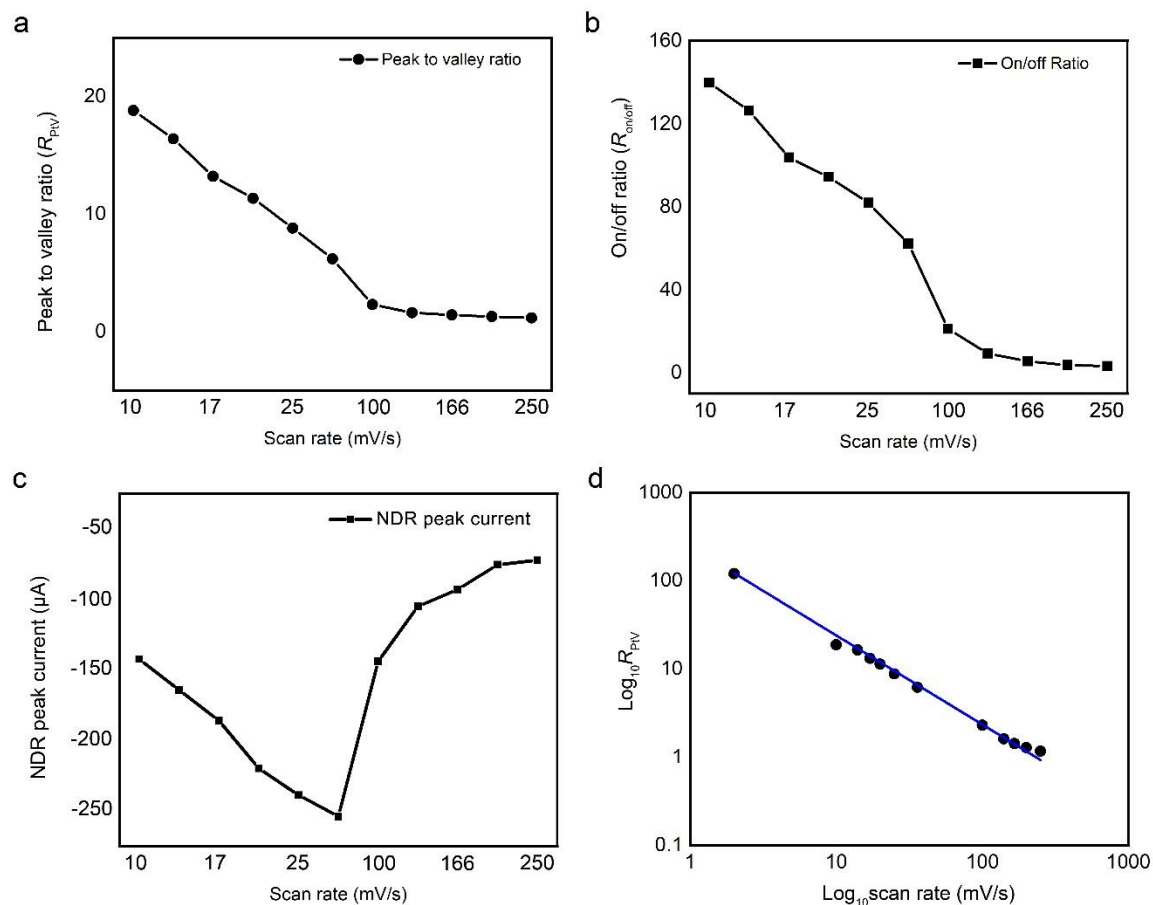
Extended Data

Extended Data Fig. 1. Energy level diagrams of the junction in switching and reset process. In switching process, H_n-HATNA turns on because a new molecular energy level appears, the midgap state (dashed red line), which changes the energy level alignment of the junction (indicated by χ) and increases the tunneling rate of the electrons. Initially, the H_0-HATNA has a large HOMO-LUMO gap and the junction is in the off state, but upon reduction (values of $n = 1\text{-}4$) the mid gap state appears lowering the tunneling barrier and the junction turns on. The midgap state disappears again upon continuous reduction ($n = 5,6$) turning the junctions off. In reset process, fully reduced H_6-HATNA oxidizes back to the initial H_0-HATNA which has a large HOMO-LUMO gap and the whole process can start again.

31
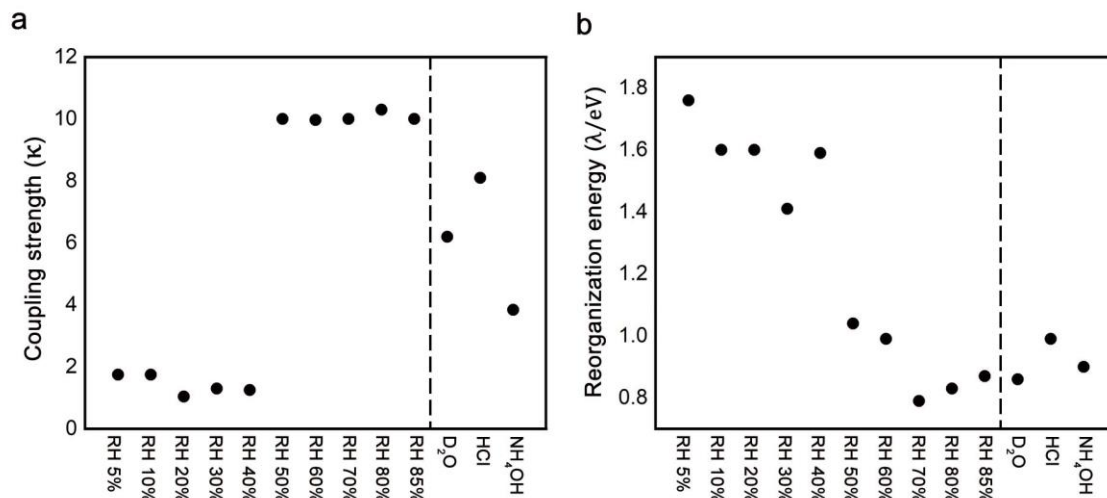
Extended Data Fig. 2. Fitting results for the parameters κ and λ. (a) κ is a multiplier describing the change in the coupling strength of the molecule to the electrodes between the on and off states. κ is close to unity t for low relative humidity (RH), but increases to almost 10 for high RH illustrating a substantial increase of the molecule-electrode coupling as a result of protonation. (b) Reorganization energy λ decreases with increasing RH illustrating how protonation is facilitated (or becomes easier) at high RH.

32

Extended Data Fig. 3. Peak-to-valley ratio (R_{PtV}) (a), on/off ratio ($R_{on/off}$), (b) and NDR peak current (c) as a function of scan rate ranging from 10 to 250 mV/s. (d) Power law dependence with slope -1.01 of R_{PtV} as a function of scan rate in $\log_{10}$ scale. This plot shows that for lower scan rates probably even larger values of R_{PtV} can be obtained.

33